

# Liquid-Like, Self-Healing Aluminum Oxide during Deformation at Room Temperature

Yang Yang,<sup>†</sup> Akihiro Kushima,<sup>†,‡,§</sup> Weizhong Han,<sup>⊥</sup> Huolin Xin,<sup>\*,||</sup> and Ju Li<sup>\*,†,‡,⊥</sup>

<sup>†</sup>Department of Nuclear Science and Engineering, Massachusetts Institute of Technology, Cambridge, Massachusetts 02139, United States

<sup>‡</sup>Department of Materials Science and Engineering, Massachusetts Institute of Technology, Cambridge, Massachusetts 02139, United States

<sup>§</sup>Department of Materials Science and Engineering, Advanced Materials Processing and Analysis Center, University of Central Florida, Orlando, Florida 32816, United States

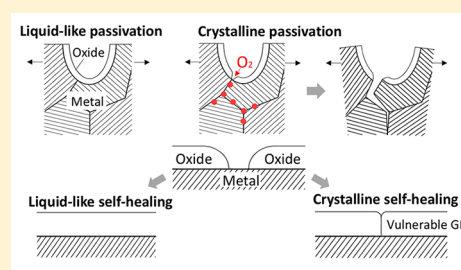
<sup>||</sup>Center for Functional Nanomaterials, Brookhaven National Laboratory, Upton, New York 11973, United States

<sup>⊥</sup>Center for Advancing Materials Performance from the Nanoscale (CAMP-Nano), State Key Laboratory for Mechanical Behavior of Materials, Xi'an Jiaotong University, Xi'an 710049, China

**S** Supporting Information

**ABSTRACT:** Effective protection from environmental degradation relies on the integrity of oxide as diffusion barriers. Ideally, the passivation layer can repair its own breaches quickly under deformation. While studies suggest that the native aluminum oxide may manifest such properties, it has yet to be experimentally proven because direct observations of the air-environmental deformation of aluminum oxide and its initial formation at room temperature are challenging. Here, we report *in situ* experiments to stretch pure aluminum nanotips under O<sub>2</sub> gas environments in a transmission electron microscope (TEM). We discovered that aluminum oxide indeed deforms like liquid and can match the deformation of Al without any cracks/spallation at moderate strain rate. At higher strain rate, we exposed fresh metal surface, and visualized the self-healing process of aluminum oxide at atomic resolution. Unlike traditional thin-film growth or nanoglass consolidation processes, we observe seamless coalescence of new oxide islands without forming any glass–glass interface or surface grooves, indicating greatly accelerated glass kinetics at the surface compared to the bulk.

**KEYWORDS:** Superplasticity, glass surface, aluminum oxide, self-healing, stress-corrosion cracking, *in situ* TEM



Alumina and silica are special oxides for passivation in that they rapidly develop under air in a glassy state with a thickness of only a few nanometers, establishing an effective barrier against further oxidation. The mechanical behavior of these surface glasses in oxidizing environment and their initial formation are interesting for understanding not only stress-corrosion cracking, but also thin-film growth<sup>1</sup> and nanoglass<sup>2</sup> kinetics. On one hand, the plasticity of metal oxide and its adherence to metal are critical for the stress-corrosion cracking (SCC) tolerance of metals.<sup>3,4</sup> If oxide at a metal crack tip (Figure 1a) breaks up under stress, and this breach is not repaired sufficiently quickly, embrittling elements such as oxygen<sup>5</sup> and hydrogen<sup>6</sup> will diffuse inward through the grain boundary network (Figure 1b), leading to internal oxidation, dynamic embrittlement (DE),<sup>7</sup> or stress-assisted grain boundary oxidation (SAGBO),<sup>5,8</sup> etc. The consequence is relocation of the crack tip to the grain boundary, propagation of intergranular cracking (Figure 1c), and greatly enhanced total oxidation rate by internal, instead of external, oxidation. An ideal passivation layer may require liquid-like superplasticity that does not fracture when elongated. Such a property is often found in glass at high temperature where viscous flow is

enabled; however, there has been little work reporting this property in ceramics at room temperature. Recently, there is growing evidence that the outside layer of polymeric and organic glasses with few nanometers thickness is in an enhanced-diffusivity state at room temperature because the glass transition temperature  $T_g$  is much smaller for thinner films.<sup>9–11</sup> Therefore, native alumina and silica may have liquid-like behaviors at room temperature.<sup>12</sup> Experimentally, the deformation process of native aluminum oxide in gas environments has never been observed at the atomic scale because of its ultrasmall thickness. Thicker aluminum oxide films grown by anodic reactions<sup>13</sup> are often used for measurements instead, whose representation of the native oxide is questionable because of the thickness dependence of mechanical behaviors. Therefore, there is a need for a high-resolution deformation technique in gas environments to verify the deformability of aluminum oxide surface glass.

**Received:** January 6, 2018

**Revised:** February 18, 2018

**Published:** February 28, 2018

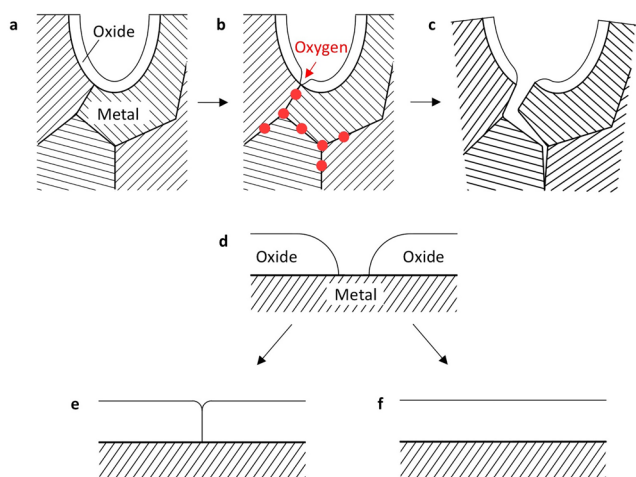


**Figure 1.** (a–c) Schematic drawing of the dynamic embrittlement process after cracking in oxide. (a) Oxide is intact and provides excellent protection of metal at a stressed crack tip. (b) Oxygen ingress to metal grain boundary due to the fracture of oxide. (c) Intergranular cracking. (d–f) Schematic illustration of the difference between solid and liquid when two oxide islands coalesce during growth. (d) Oxide nucleates as an island on the metal surface. (e) An interface and a groove are formed when two islands meet, which applies to the thin-film growth (either crystalline or amorphous) and nanoglass consolidation process. (f) Seamless coalescence of islands, indicative of the liquid-like behavior.

Also, at sufficiently high strain rates, when the oxide finally breaks, and fresh aluminum is exposed, it still remains unclear how the new oxide is formed and then connected to the new/old oxide nearby. During the nucleation stage, alumina will grow as islands (Figure 1d) which by nature are nanoglass.

Previous experiments on thin-film growth, either crystalline<sup>1,14</sup> or amorphous,<sup>15,16</sup> as well as nanoglass fabrication<sup>2,17</sup> indicate that glass–glass interfaces (GGIs) with surface grooves will form when two nanoglass islands coalesce (Figure 1e). The surface groove is an indication of finite GGI free energy that needs to be balanced by surface tension of the cusp of the surface, according to Young's equation. GGI may not be as resistant to oxygen and metal diffusion as the glass itself. Furthermore, GGIs and grooves are less mechanically robust, and under stress, further fracture will likely proceed along them in the SCC context. If alumina/silica is liquid-like, there should be no GGI nor grooves when two oxide islands meet (Figure 1f); however, there is a lack of experimental confirmation on this due to the difficulty in preparing fresh (i.e., unoxidized) and uncontaminated metal surfaces in a TEM. Observing the initial formation process of glassy oxide at the atomic scale is experimentally challenging, and it has been rarely reported in the literature.

The recently developed environmental transmission electron microscopy (ETEM) technique has been successfully used to visualize initial oxidation in copper.<sup>18,19</sup> While previous experiments are conducted without applying external stress, in this paper we will utilize ETEM to visualize the simultaneous deformation and oxidation process in aluminum at the atomic scale. We will show that native aluminum oxide can deform superplastically at room temperature under oxygen gas environment without thickness reduction, as a result of concurrent shear relaxation by enhanced bond-switching in thin films and self-healing by dynamic oxidation. When increasing the strain rate, we are able to expose fresh aluminum surface and directly probe subsequent seamless self-healing in the oxide. The strain-rate sensitivity discovered here agrees well

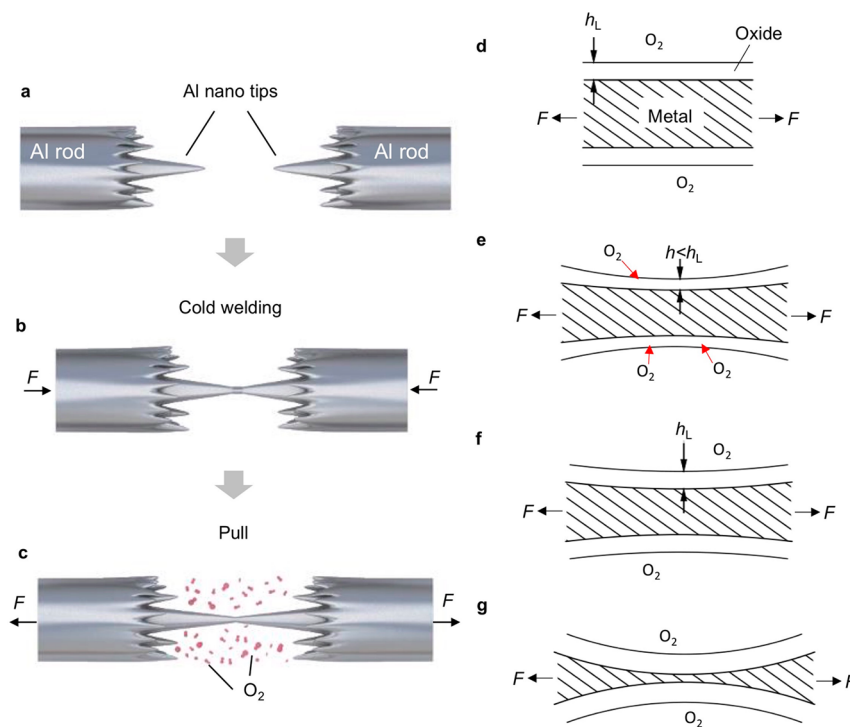


**Figure 2.** Illustration of the environmental deformation of aluminum oxide. (a–c) Schematic drawing of the experimental configuration. (a) Two Al rods with nanotips are aligned. (b) Their longest tips are contacted and then cold-welded. (c) The junction is then pulled in oxygen environment. (d–g) Schematic illustration of the concurrent oxidation and deformation process of aluminum in oxygen environment.

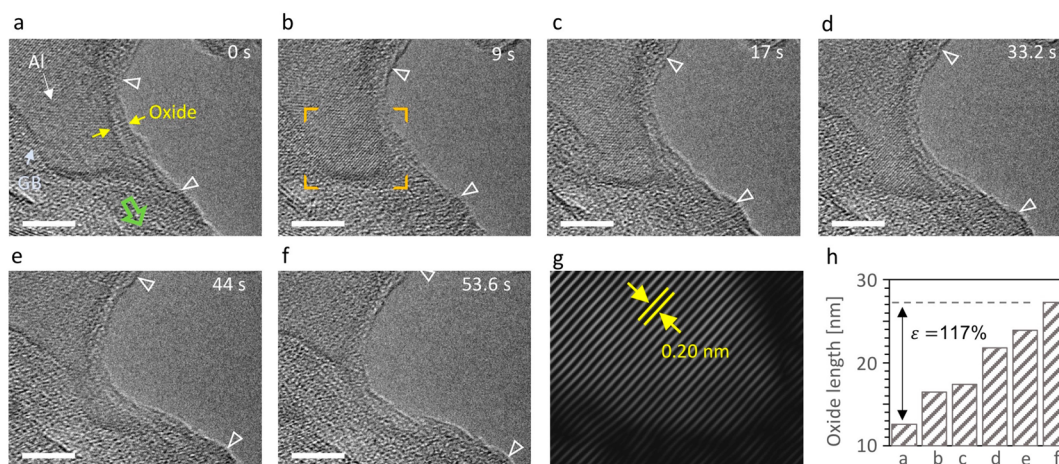


**Figure 3.** Liquid-like superplasticity of aluminum oxide layer at room temperature (Movie S1, Supporting Information). (a–f) Sequential TEM images showing the superelongation and self-healing process of aluminum oxide when stretched in  $2 \times 10^{-6}$  Torr oxygen environment; oxide between the two white triangular marks in parts a–f are the segment being stretched. The green arrow in part a represents the stretching direction. An aluminum grain boundary (GB) is pointed out by a light-blue arrow in part a. (g) Filtered high-resolution image for the orange-boxed region in part b, showing (200) crystalline planes. The oxide length (surface length between two triangular markers) for parts a–f are plotted in part h, showing a maximum strain of 117%. All scale bars, 5 nm.

with MD modeling results by Sen et al.<sup>12</sup> and is analogous to the one proposed for silica glass nanowires.<sup>20</sup>

Our nanoscale environmental deformation setup is illustrated in Figure 2. Two selected nanotips on Al rods are aligned in the ETEM instrument under high vacuum (Figure 2a). One tip will then approach the other gradually. When their distance is around 3.1 nm, the two tips will jump into contact<sup>21</sup> because of the Casimir attraction force.<sup>22</sup> Further compressing the two tips leads to cold-welding<sup>23</sup> (Figure 2b). Afterward, pure oxygen gas will be injected in the TEM sample chamber. The deformation process of aluminum oxide at atomic resolution will then be probed when moving one Al rod away gently (Figure 2c).

When the strain rate is low, our observation of simultaneous oxidation and deformation process is summarized schematically in Figure 2 d–g. The superplasticity is a consequence of “viscous flow” in aluminum oxide as well as dynamic self-healing by oxidation. An aluminum tip with native oxide shell is pulled under oxygen atmosphere at low strain rate (Figure 2d). Similar to other nanoscopically confined glass formers,<sup>9,20</sup> the ion mobility is greatly enhanced at the near-surface region (sub-10 nm) which drives rapid bond-switching to repair surface flaws generated by deformation. Meanwhile, the chemisorbed oxygen molecules near the surface mediate healing of broken bonds<sup>12</sup> (Figure 2e), adding to the thickness of oxide  $h$  when  $h$  is smaller than the limiting thickness  $h_L$ . The interplay between these two processes leads to the superelongation in aluminum oxide shell without fracture and reduction in oxide thickness (Figure 2f). This mechanism can be deactivated when the fresh aluminum beneath the oxide is depleted (Figure 2g). More discussion about the reduced  $T_g$  in alumina surface is provided in section 1 of the Supporting Information.

Figure 3a–h and Movie S1, Supporting Information, present experimental evidence for the process above, showing a typical deformation process of aluminum oxide in  $2 \times 10^{-6}$  Torr oxygen environment and at a moderate strain rate ( $\sim 2.2 \times 10^{-2} \text{ s}^{-1}$ ). A segment of aluminum oxide being stretched is marked by the white-triangle locations as fiducial markers. When the sample is pulled along the direction indicated by the green arrow (Figure 3a), the oxide segment is uniformly elongated (Figure 3b–f). A strain of 117% is reached at  $t = 53.6$  s (Figure

3f,h); however, surprisingly neither cracks nor pores are generated inside the glass or at the metal–glass (M–G) interface throughout the whole process. The stretching process of aluminum oxide on metal is just like liquid spreading on a surface. The oxide thickness  $h$  may slightly reduce because of an occasional higher strain rate (Figure 3d) but can soon recover to  $h_L$  when the strain rate decreases (Figure 3e). Thus, the oxide thickness is almost uniform and unchanged because of the rapid growth of oxide. It is also noteworthy that the oxide segment was straight at  $t = 0$  s, but it became more and more curved after necking in metal. While the severely curved M–G interface assumes a dramatic variation of aluminum surface inclinations, it is remarkable that alumina can keep matching the deformation of metal and attach perfectly to protect the surface. Such a liquid-like, isotropic, complete wetting feature, which originates from the amorphous nature of native aluminum oxide, is pivotal for a mechanically robust protection layer.

We want to emphasize that there is no elongation limit to failure for aluminum oxide at low strain rate unless metal is depleted. To further demonstrate this, a tearing experiment is performed in  $1.5 \times 10^{-1}$  Torr oxygen environment. This differs from tensile testing in that internal fracture in the metal grain is being generated. In this experiment, a volume of about 25 000 nm<sup>3</sup> is torn away from the matrix, but the oxide is always continuous and attaching well to metal throughout the experiment (Supporting information, section 2, Movie S2, and Figure S1). The uninterrupted coverage of fracture surface by a thick (>1 nm) oxide is probably due to a “viscous-flow-like” behavior. Although superelongation was reported in nanoscale metallic glass<sup>24</sup> and silica glass systems,<sup>20</sup> it has not been reported in metal oxide glass systems. Our observation here indicates that nano-scale-thin coatings of metal oxide glass can have significantly improved deformability. Note that our conclusion is already based on the thicker<sup>25</sup> alumina film ( $\sim 3$  nm) that is present in practical environments.

While it is intriguing to see the ductility of the ceramic glass matching that of the metal underneath at room temperature and low strain rates, when the strain rate is much higher, fracture will occur in the glass, exposing clean aluminum surface

(Supporting Information, [Movie S3](#) and [Figure S2](#)). The key here is to find out how quickly such a true “breach in the wall” can be repaired, as a breach can hit the metal–metal grain boundary intersection, and rapid internal oxidation and degradation can occur ([Figure 1a–c](#)). Our “mechanical break junction” setup mimics the local environment of a stressed crack tip in air, and is also a perfect setup for the study of the initial oxidation. Aluminum oxide can hardly be reduced by heating in  $H_2$ . In contrast to conventional methods to prepare clean surfaces of aluminum<sup>26</sup> such as argon ion sputtering, our mechanical break junction approach is more practical for *in situ* TEM experiments.

[Figure 4a–f](#) shows time-sequence HRTEM images of the oxidation process on a clean aluminum surface created by the

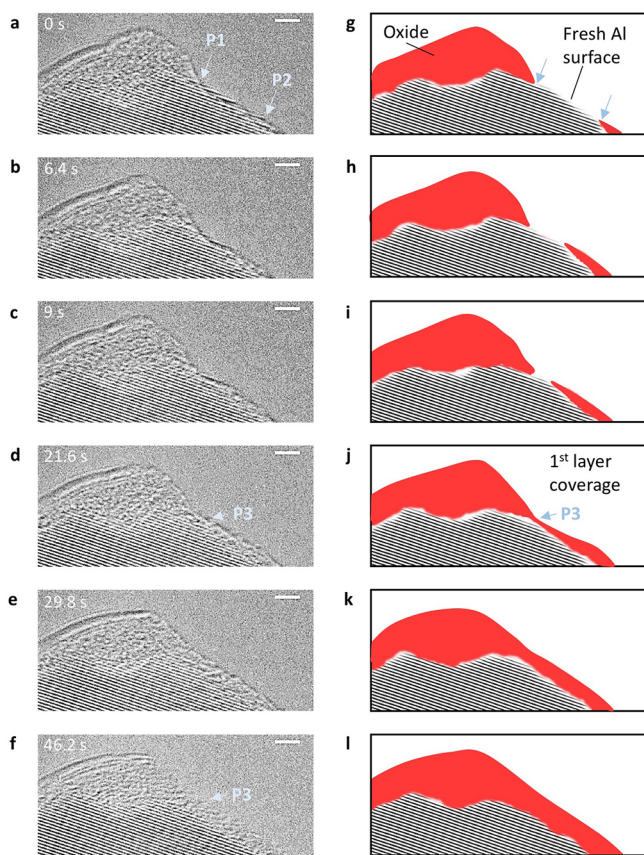


**Figure 4.** Initial oxidation of pure aluminum at room temperature (Supporting Information, [Movie S4](#)). (a–f) Sequential HRTEM images showing the oxidation process at oxygen pressure of  $3.6 \times 10^{-6}$  Torr. (g–l) Processed images of parts a–f to indicate different phase distribution: the aluminum lattice planes, shown by black lines, are filtered images of parts a–f using a set of aluminum (111) diffraction spots; the oxide is shown by red color. All scale bars, 2 nm.

fracture, accompanied by their individual filtered images in [Figure 4g–l](#) with better resolution of the phase boundaries. (See more details of the process in the Supporting Information, [Movie S4](#); the filtration method is introduced in section 3.) Pure  $O_2$  at a pressure of  $3.6 \times 10^{-6}$  Torr is maintained during the whole process. Interestingly, new oxide tends to nucleate right next to the old oxide (i.e., triple junction of glass–metal–vapor interfaces, as depicted by P1 and P2 in [Figure 4a,g](#).) and then spread out to cover the unoxidized fresh metal, instead of growing uniformly on the fracture surface. Oxide will progress

in this manner to cover the entire fracture surface, and meanwhile, new oxide becomes thicker by motion of the M–G interface (i.e., direct transformation from metal lattice to oxide phase mediated by oxygen subsurface incorporation). This is significantly different from the adatom mechanism observed in pure copper.<sup>18</sup> [Figure 4d,j](#) shows the first-layer coverage on the fracture surface by oxide. The gradient of oxide thickness is evident from the merging point (P3 in [Figure 4j](#)) to the oxidation starting point (P1 and P2); however, it will soon disappear leaving a uniform oxide layer on the fracture surface ([Figure 4f,l](#)). Furthermore, the interface between the old oxide and the new oxide (at P1 and P2) as well as the interface where the new oxides merge (at P3) are indistinguishable and contain *no grooves*, resembling the behaviors of liquid. This is particularly intriguing since it is significantly different from amorphous thin films evaporated on a substrate at room temperature.<sup>16</sup> Previous experiments have shown that the surface roughness (corresponding to the depth of grooves) of evaporated metallic glass thin films can be reduced either by heating a thick film above  $T_g$  for relaxation<sup>27</sup> or decreasing the film thickness,<sup>16</sup> suggesting that  $T_g$  may be smaller when film thickness decreases. However, even for a thin film of 0.8 nm thickness, grooves are still apparent.<sup>15</sup> Our observation of a grooveless surface in 2 nm thick alumina illustrates the liquid-like behavior during the glass thin-film growth process. Another piece of evidence showing the disappearance of the GGI during the cold-welding process is illustrated in the Supporting Information, section 4 and [Figure S3](#). In the context of high-strain-rate deformation mimicking the crack-tip environment, the self-healing feature of aluminum oxide manifests itself by the rapid recovery of a conformal and homogeneous oxide layer at the fracture surface. This is of great importance to SCC since any heterogeneity led by a mismatch between oxide scales, for example, oxide-oxide grain boundaries or phase boundaries, may introduce tensile residual stress (well-known in thin-film growth) that buries a seed for future cracking/spallation. The residual stress in surface glass here is expected to be small and rapidly decaying because of the facile diffusive relaxation kinetics of surface glass by reduced  $T_g$ .<sup>9–11</sup> Note that the internal stress may not always be deleterious if it is compressive.

In this vein, we want to point out two distinctive features. One of them is surface smoothing/relaxation which occurs not only at the M–G interface but also at the glass–vapor (G–V) interface. [Figure S4a,b](#), in the Supporting Information, shows the evolution of an oxide fracture surface. The sharp tip at  $t = 0$  s is the final detach point after the tearing experiment. After blanking e-beam for 310 s, the tip becomes blunted to minimize the roughness of the G–V interface. In contrast, crystalline copper oxide grains grow as small hills on copper metal surface,<sup>18</sup> and magnesium oxide developed strongly anisotropic surface features such as zigzag facets (Supporting Information, [Figure S5](#)). The other feature is the conformability of aluminum oxide formed on highly curved surface, as revealed by [Figure S4c,d](#), in the Supporting Information. Despite that the  $90^\circ$  curved fracture surface of aluminum possesses abundant surface inclinations, the oxide formed afterward is uniform and smooth. The two features discussed above are important for understanding friction and wear, as well as thermal and electrical contact resistances since the nano-/atomic-scale surface asperities control the state, or “quality”, of the true contact area.<sup>28</sup> Also, the surface roughness of native aluminum oxide may have an impact on the effective modulus of aluminum thin films.<sup>29</sup>

This work reveals liquid-like superplasticity and seamless, isotropic self-healing features of aluminum oxide in gaseous oxygen environments at room temperature. The accelerated glass surface kinetics of native alumina is not likely to be a radiation damage artifact of the imaging electron beam. We have performed a series of experiments and analyses to investigate the influence of electron beam (Supporting Information, section 5).

Our findings have important implications for the fundamental understanding of friction, lubrication, adhesion, electrical and thermal contact resistances, and stress-corrosion cracking on surfaces of aluminum or aluminum alloys as well as aluminum oxide coatings. Coatings by amorphous aluminum oxide, for instance, by atomic layer deposition (ALD) method,<sup>30</sup> have become popular for anticorrosion<sup>31</sup> and fabrication of micro-/nanodevices.<sup>32</sup> Our discovery suggests that a bilayer coating containing both aluminum and aluminum oxide may have better mechanical performance in an oxidative environment than a standalone layer of aluminum oxide because of the triggered self-healing function. In addition, the discovery of seamless growth of alumina thin films on aluminum may benefit the exploration of better control of interfaces in vapor-deposited thin films and nanoglass. Investigations in other nanoscopically thin films of glassy metal oxide will be worthwhile to further unravel their unique properties. Lastly, our *in situ* technique that combines ETEM with a nanostraining holder is demonstrated to be a powerful tool in studying SCC and initial oxidation in metals, enabling visualization of chemically and/or mechanically induced phase transformations at atomic resolution.

**Methods.** The materials investigated in this work are extra pure (99.99%) aluminum rods (diameter: 0.01 in.) from ESPI Metals. To obtain thin aluminum TEM samples with satisfactory electron transparency, we prepared aluminum nanotips at one end of a pure aluminum rod by simultaneously drawing and cutting aluminum rods in air at room temperature. A natural oxide layer around 2–3 nm in thickness will develop on the surface of aluminum nanotips instantly. Compared to nanostructured mechanical testing samples fabricated by focused ion beam (FIB) which will introduce irradiation damage and contamination (Ga and Pt), our samples are much cleaner and more realistic. The *in situ* experiments were conducted inside an FEI Titan environmental TEM, working at a voltage of 300 kV. Nanoscale mechanical deformation was enabled by a Nanofactory scanning tunneling microscope (STM) holder.

## ■ ASSOCIATED CONTENT

### 📄 Supporting Information

The Supporting Information is available free of charge on the ACS Publications website at DOI: 10.1021/acs.nanolett.8b00068.

Additional discussion, comparison of  $T_g$  values, tearing experiment, image filtering process, and supplementary HRTEM images (PDF)

Movie S1: pulling aluminum oxide in  $2 \times 10^{-6}$  Torr oxygen environment at room temperature (AVI)

Movie S2: tearing experiment performed in  $1.5 \times 10^{-1}$  Torr oxygen environment at room temperature (AVI)

Movie S3: preparation of clean aluminum surface by pulling the junction at high strain rate (AVI)

Movie S4: initial oxidation on aluminum fracture surface under  $3.6 \times 10^{-6}$  Torr oxygen environment (AVI)

Movie S5: ultra-low-dose-rate experiment for the observation of tearing in an Al nano tip: oxygen pressure,  $1.5 \times 10^{-1}$  Torr; dose rate,  $92 \text{ e}^-/(\text{\AA}^2 \text{ s})$  (AVI)

## ■ AUTHOR INFORMATION

### Corresponding Authors

\*E-mail: [hxin@bnl.gov](mailto:hxin@bnl.gov).

\*E-mail: [liju@mit.edu](mailto:liju@mit.edu).

### ORCID

Yang Yang: 0000-0002-0025-5914

Weizhong Han: 0000-0001-7982-4042

Ju Li: 0000-0002-7841-8058

### Author Contributions

J.L., Y.Y., and H.L.X. conceived and designed the project. Y.Y. and A.K. conducted the experimental work. J.L. and Y.Y. wrote the paper. All authors contributed to discussions of the results.

### Notes

The authors declare no competing financial interest.

## ■ ACKNOWLEDGMENTS

We acknowledge support from NSF DMR-1410636. We also thank Eric Stach from University of Pennsylvania; Sidney Yip, Michael Short, Mingda Li, Zhe Shi, and Alicia Elliott from MIT; Dong Su from Brookhaven National Laboratory; Penghan Lu from Forschungszentrum Juelich; Yuecun Wang from Xi'an Jiaotong University; and Weiwei Xia from Southeast University for helpful discussions. This research used resources of the Center for Functional Nanomaterials, which is a U.S. DOE Office of Science Facility, at Brookhaven National Laboratory under Contract DE-SC0012704.

## ■ REFERENCES

- (1) Thompson, C. V.; Carel, R. *J. Mech. Phys. Solids* **1996**, *44* (5), 657–673.
- (2) Gleiter, H. *Beilstein J. Nanotechnol.* **2013**, *4* (1), 517–533.
- (3) Schütze, M. *Mater. Sci. Technol.* **1990**, *6* (1), 32–38.
- (4) Robertson, J.; Manning, M. I. *Mater. Sci. Technol.* **1990**, *6* (1), 81–92.
- (5) Yamaura, S.; Tsurekawa, S.; Watanabe, T. *Mater. Trans.* **2003**, *44* (7), 1494–1502.
- (6) Chen, Y.-S.; Haley, D.; Gerstl, S. S. A.; London, A. J.; Sweeney, F.; Wepf, R. A.; Rainforth, W. M.; Bagot, P. A. J.; Moody, M. P. *Science (Washington, DC, U. S.)* **2017**, *355* (6330), 1196–1199.
- (7) Misra, R. D. K.; Prasad, V. S.; Rao, P. R. *Scr. Mater.* **1996**, *35* (1), 129–133.
- (8) Bricknell, R. H.; Woodford, D. a. *Metall. Trans. A* **1981**, *12* (9), 1673–1680.
- (9) Ellison, C. J.; Torkelson, J. M. *Nat. Mater.* **2003**, *2* (10), 695–700.
- (10) Fakhraai, Z.; Forrest, J. A. *Science (Washington, DC, U. S.)* **2008**, *319* (5863), 600–604.
- (11) Yang, Z.; Fujii, Y.; Lee, F. K.; Lam, C.; Tsui, O. K. C. *Science (Washington, DC, U. S.)* **2010**, *328* (5986), 1676–1679.
- (12) Sen, F. G.; Alpas, A. T.; van Duin, A. C. T.; Qi, Y. *Nat. Commun.* **2014**, *5*, 1–9.
- (13) Bradhurst, D. H.; Llewelyn Leach, J. S. *J. Electrochem. Soc.* **1966**, *113* (12), 1245.
- (14) Mullins, W. *Acta Metall.* **1958**, *6* (6), 414–427.
- (15) Mayr, S. G.; Moske, M.; Samwer, K. *Europhys. Lett.* **1998**, *44* (4), 465–470.
- (16) Mayr, S. G.; Samwer, K. *Phys. Rev. Lett.* **2001**, *87* (3), 361051–361054.

- (17) Jing, J.; Krämer, A.; Birringer, R.; Gleiter, H.; Gonser, U. *J. Non-Cryst. Solids* **1989**, *113* (2–3), 167–170.
- (18) Zhou, G.; Luo, L.; Li, L.; Ciston, J.; Stach, E. A.; Yang, J. C. *Phys. Rev. Lett.* **2012**, *109* (23), 1–5.
- (19) Li, L.; Luo, L.; Ciston, J.; Saidi, W. A.; Stach, E. A.; Yang, J. C.; Zhou, G. *Phys. Rev. Lett.* **2014**, *113* (13), 1–5.
- (20) Luo, J.; Wang, J.; Bitzek, E.; Huang, J. Y.; Zheng, H.; Tong, L.; Yang, Q.; Li, J.; Mao, S. X. *Nano Lett.* **2016**, *16* (1), 105–113.
- (21) Sun, J.; He, L.; Lo, Y.-C.; Xu, T.; Bi, H.; Sun, L.; Zhang, Z.; Mao, S. X.; Li, J. *Nat. Mater.* **2014**, *13* (11), 1007–1012.
- (22) Zhang, X.; He, Y.; Sushko, M. L.; Liu, J.; Luo, L.; De Yoreo, J. J.; Mao, S. X.; Wang, C.; Rosso, K. M. *Science (Washington, DC, U. S.)* **2017**, *356* (6336), 434–437.
- (23) Lu, Y.; Huang, J. Y.; Wang, C.; Sun, S.; Lou, J. *Nat. Nanotechnol.* **2010**, *5* (3), 218–224.
- (24) Luo, J. H.; Wu, F. F.; Huang, J. Y.; Wang, J. Q.; Mao, S. X. *Phys. Rev. Lett.* **2010**, *104* (21), 1–4.
- (25) Cai, N.; Zhou, G.; Müller, K.; Starr, D. E. *Phys. Rev. B: Condens. Matter Mater. Phys.* **2011**, *84* (12), 1–6.
- (26) Jona, F. *J. Phys. Chem. Solids* **1967**, *28* (11), 2155–2160.
- (27) Reinker, B.; Moske, M.; Samwer, K. *Phys. Rev. B: Condens. Matter Mater. Phys.* **1997**, *56* (15), 9887–9893.
- (28) Li, S.; Li, Q.; Carpick, R. W.; Gumbsch, P.; Liu, X. Z.; Ding, X.; Sun, J.; Li, J. *Nature* **2016**, *539* (7630), 541–545.
- (29) Saif, M. T. a.; Zhang, S.; Haque, a.; Hsia, K. J. *Acta Mater.* **2002**, *50* (11), 2779–2786.
- (30) Ritala, M. *Science (Washington, DC, U. S.)* **2000**, *288* (5464), 319–321.
- (31) Ritala, M.; Niinistö, J. In *ECS Transactions*; ECS, 2009; Vol. 25, pp 641–652.
- (32) Tripp, M. K.; Stampfer, C.; Miller, D. C.; Helbling, T.; Herrmann, C. F.; Hierold, C.; Gall, K.; George, S. M.; Bright, V. M. *Sens. Actuators, A* **2006**, *130–131*, 419–429.

# Supplementary Materials for

## Liquid-like, self-healing aluminum oxide during deformation at room temperature

Yang Yang<sup>1</sup>, Akihiro Kushima<sup>1,2,3</sup>, Weizhong Han<sup>5</sup>, Huolin Xin<sup>4\*</sup>, Ju Li<sup>1,2\*</sup>

<sup>1</sup> *Department of Nuclear Science and Engineering, Massachusetts Institute of Technology, Cambridge, Massachusetts 02139, USA*

<sup>2</sup> *Department of Materials Science and Engineering, Massachusetts Institute of Technology, Cambridge, Massachusetts 02139, USA*

<sup>3</sup> *Department of Materials Science and Engineering, Advanced Materials Processing and Analysis Center, University of Central Florida, Orlando, Florida 32816, USA*

<sup>4</sup> *Center for Functional Nanomaterials, Brookhaven National Laboratory, Upton 11973, USA*

<sup>5</sup> *Center for Advancing Materials Performance from the Nanoscale (CAMP-Nano), State Key Laboratory for Mechanical Behavior of Materials, Xi'an Jiaotong University, Xi'an 710049, China*

\*E-mail: [hxin@bnl.gov](mailto:hxin@bnl.gov) (H.L.X.), [liju@mit.edu](mailto:liju@mit.edu) (J.L.)

### **This PDF file includes:**

Materials and Methods  
Supplementary Text (Section 1 to 5)  
Figs. S1 to S7  
Captions for Movies S1 to S5  
Reference for the supplementary materials

### **Other Supplementary Materials for this manuscript includes the following:**

Movies S1 to S5

## Materials and Methods

The materials investigated in this work are extra pure (99.99%) aluminum rods (diameter: 0.01 in.) from ESPI Metals. To obtain thin aluminum TEM samples with satisfactory electron transparency, we prepared aluminum nanotips at one end of a pure aluminum rod by simultaneously drawing and cutting aluminum rods in air and at room temperature. A natural oxide layer around 2-3 nm in thickness will develop on the surface of aluminum nanotips instantly. Compared to nanostructured mechanical testing samples fabricated by focused ion beam (FIB) which will introduce irradiation damage and contamination (Ga and Pt), our samples are much cleaner and more realistic. The *in-situ* experiments were conducted inside an FEI Titan environmental TEM instrument, working at a voltage of 300 kV. Nanoscale mechanical deformation was enabled by a Nanofactory scanning tunneling microscope (STM) holder.

## Supplementary Text

### 1. Reduced $T_g$ in thin films

The superplasticity in native alumina is led by two reasons: (1) Reduced  $T_g$  at surface region; (2) The chemisorbed oxygen helps repair the broken bond at surface, as proved by the molecular dynamic simulations<sup>1</sup>.

When comparing the reduced  $T_g$  between different materials, we consider the homologous temperature. Define:

$$k = \frac{T_{g,bulk} - T_g}{T_m} \quad (1)$$

where  $T_m$  is the melting point measured in Kelvin unit. Here we present our calculation results of  $k$  for two different materials in the table below:

Table 1: Comparison of  $T_g$  of thin films in PS and native alumina

Material	Film thickness [nm]	Melting point		Bulk		Thin film		$k$
		$T_m$ [K]	Source	$T_{g,bulk}$ [K]	Source	$T_g$ [K]	Source	
Polystyrene (PS)	5	513	Ref. <sup>2</sup>	374	Ref. <sup>3</sup>	206	Calculated by Eq. (2)	0.32
Amorphous $Al_2O_3$	3.1	2327	Ref. <sup>4</sup>	973	Ref. <sup>5</sup>	300	Room temperature	0.29

The  $T_g$  for PS of 5 nm thick is calculated using the equation<sup>3</sup>:

$$T_g(h) = T_{g,bulk}[1 - (\frac{A}{h})^\delta] \quad (2)$$

where  $h$  is film thickness,  $A$  is a characteristic length (3.2 nm) and  $\delta = 1.8$ .

From Table 1, we can find that  $k$  for PS and Amorphous  $Al_2O_3$  are at the same order.

Also, as revealed by MD simulations<sup>1</sup>, the chemisorbed oxygen can help repair the broken bonds in alumina surfaces. This phenomenon is much stronger in ambient conditions where the oxygen partial pressure is much higher than that in our experiment. What is more, the chemical reaction (oxidation) itself can stimulate rapid surface kinetics, namely the chemical-induced creep<sup>6</sup> (in contrast to “thermal-induced creep”).

## 2. Tearing experiment

A tearing experiment is conducted under  $1.5 \times 10^{-1}$  Torr oxygen environment. This process is recorded in Supplementary Movie S2. Supplementary Figure S1 shows the time-sequence HRTEM images of it. A probe (left bottom corner in Figure S1a) is pushing an aluminum nanotip whose filtered image (Figure S1k) reveals that the whole part in the image is a single crystal. The aluminum tip will be torn along the yellow dashed line shown in Figure S1a thus the part below the line (volume estimated about  $25,000 \text{ nm}^3$ ) will be torn away at the end. The original thickness (limiting thickness  $h_L$ ) of oxide is around 2.9 nm, as indicated in Figure S1c at point B. Fracture in aluminum tip will first occur at point A shown in Figure S1b. As the tearing progresses, the oxide is always conformal and kept attached to the metal. No pores are visible at the M-G interface. The new oxide on fracture surface, is less than the limiting thickness at the beginning of their birth, but will eventually reach the limiting thickness by dynamic oxidation (Compare point C in Figure S1e and S1h, or point D in Figure S1f and Figure S1i.). After the tearing experiment, Figure S1j shows a conformal oxide on the new M/G interface.

During the tearing experiments, the oxide at beginning is formed in ambient conditions outside the microscope, and the thickness is  $\sim 3$  nm. Even deformed at low pressure ( $1.5 \times 10^{-1}$  Torr oxygen), the thickness of the oxide does not significantly reduce. So, our observation is already based on the *thicker* alumina film that present in practical environments. Also, we expect that at higher oxygen pressure, this surface kinetics of alumina can be further accelerated.

## 3. The filtering process for the initial oxidation

To make the phase boundaries clearer in Figure 4a-f, we adopt the following methods to create filtered images.

- 1) The lattice lines shown in Figure 4g-l are obtained by first doing FFT of Figure 4a-f and then select the (111) diffraction spots to perform inverse FFT;

- 2) The oxide shown in Figure 4g-l are obtained by detecting the oxide boundaries in Figure 4a-f using image contrast and then painted with red color.

#### 4. Disappearance of GGI during the cold-welding process

We artificially created thick oxide ( $h > h_c$ ) on two aluminum nanotips and brought them to contact to each other. It is found that right after they jumped to contact, a joint that looks like liquid-necking is formed. Glass-glass interface (GGI), i.e. merging interface, is evident at the beginning (indicated by white arrow in Figure S3b). However, the GGI will soon vanish (Figure S3c). The necking at contact and the disappearance of GGI after contact reveal a liquid-like characteristic of oxide.

#### 5. Effect of electron beam

We have performed a series of experiments and analysis to exclude the effect of e-beam:

1. The dose rate of our imaging beam is below  $5200 \text{ e}^-/(\text{\AA}^2 \cdot \text{s})$ , which is already lower than many of the other low-dose-rate *in-situ* TEM experiments<sup>7</sup>.
2. The pressure  $\times$  time for the completion of oxidation in our experiment (Figure 4 in manuscript) is around  $3.6 \times 10^{-6} \text{ Torr} \times 0.8 \text{ min} = 2.7 \times 10^{-6} \text{ Torr-min}$ , close to that reported in previous literatures<sup>8</sup> ( $2.3 \times 10^{-6} \text{ Torr-min}$ ).
3. We performed blanked beam experiment for both deformation and initial oxidation experiments.

##### 3.1 Tearing experiment:

We first cold-weld Al tips, as shown in Figure S6a. We then blank the beam, and move the tip at bottom (enclosed by green line) to left. By doing so, the tip on top is being torn. After 43 seconds, we reopen the beam. Figure S6b is the image taken right after we reopen the beam. The point A is the beginning point of fracture during the tearing experiment. During the tearing, the strain rate gradually increases, leading to a gradual decrease in oxide thickness. When the fracture point reach B, because the necking is already significant, the strain rate suddenly ramps to a very high value, leading to final detach at point C. The continuous oxide between A and B is an indication of the liquid-like behavior in alumina thin films. [Note that during the blanked beam experiment, it is much more challenging to control the strain rate accurately.]

##### 3.2 Initial oxidation on fresh surface

We also performed a blanked beam experiment in which we take a snapshot after each 30-seconds-long blanked-beam period. At the beginning, there are already some oxide near the fresh surface that are grown under e-beam. The results in Figure S7 show that

alumina indeed grows near the pre-existing oxide and slowly merges, instead of growing uniformly on fresh surface. Also, the thickness and morphology of oxide grown on the fresh Al surface without e-beam is similar to the oxide grown under e-beam. As a result, the oxide layer at the end is conformal and smooth.

- 4 Ultralow dose rate experiment for observation of alumina deformation: we decreased the dose rate to  $92 \text{ e}^-/(\text{\AA}^2\cdot\text{s})$  and used defocus to increase the contrast between oxide and metal. The *in-situ* movie (supplementary Movie S5) shows that the oxide is always continuous when we tear an Al grain out of an Al tip.

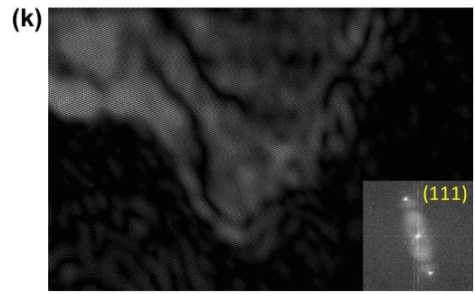
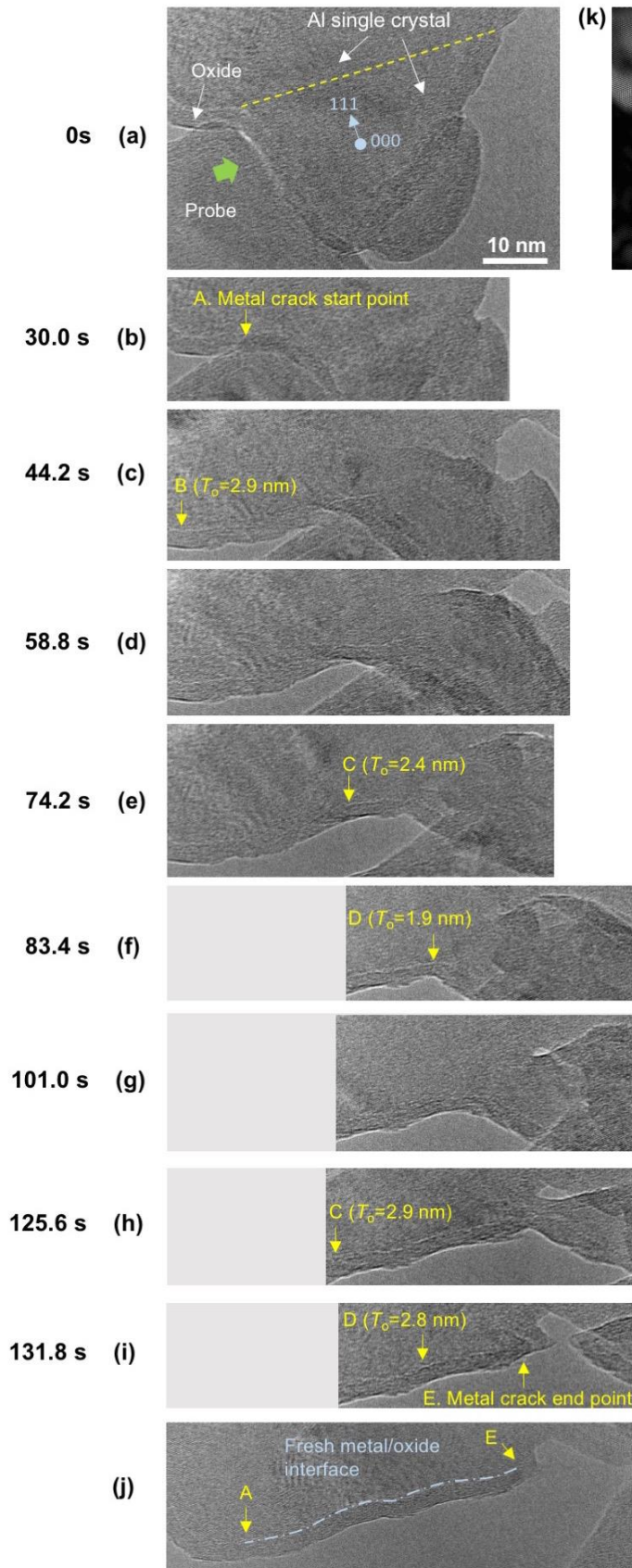


**Figure S1.**

Tearing experiment under  $1.5 \times 10^{-1}$  Torr oxygen environment. (a-j) Time-sequence HRTEM images during the deformation process. (a) The pushing direction of the probe is indicated by the green arrow. (b) Tearing starts, and the metal at point A will split into two parts. (c) The oxide thickness at point B, which is not affected by the tearing, is showing a limiting thickness of 2.9 nm. (i) Final detach point is named point E. (j) The new-born metal/oxide interface is shown by the dot-dashed line between points A and E. (k) Filtered image of (a) using a set of (111) diffraction spots.

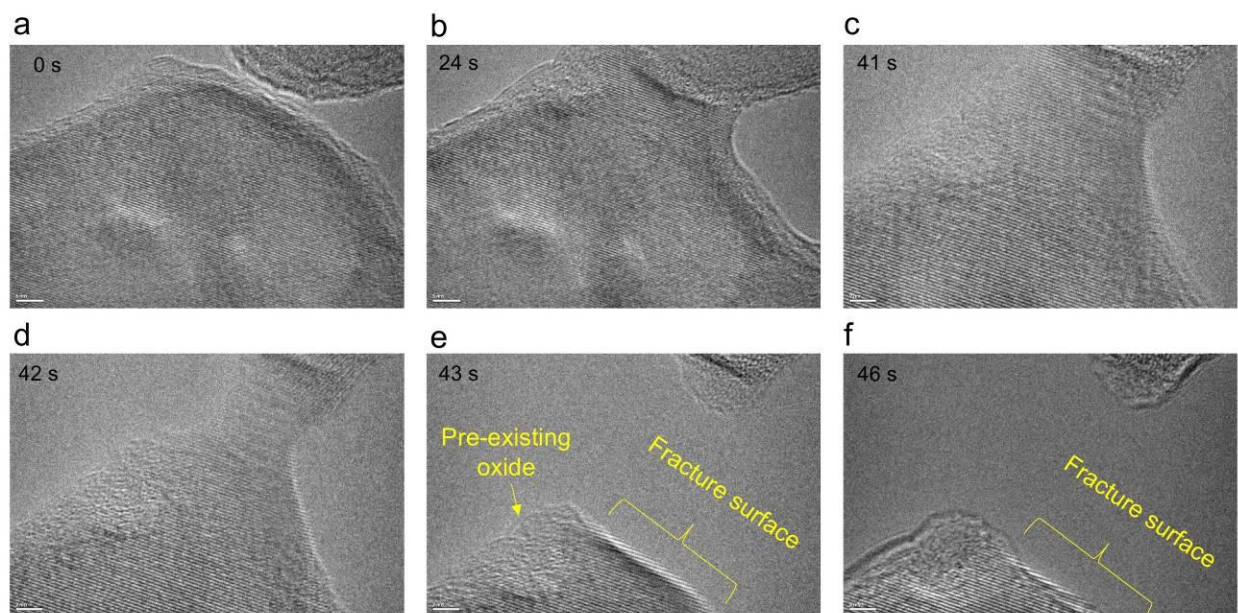


**Figure S2.**

“Mechanical break junction” approach for preparation of fresh metal surface in TEM. **a-b**, Cold welding of two aluminum nano tips in vacuum. **c-d**, Pull the junction rapidly. The aluminum nano-tip exhibits liquid-like superplastic behavior during stretching, while its crystalline structure still maintains (See the clear lattice in **c** and **d**). A rough estimation shows that the Al lattice strain is only 0.88%, comparing (c) and (f). The huge overall deformation in metal is accomplished by rapid surface diffusion<sup>7</sup>. **e**, Because the oxide behaves like a ‘super glue’, fracture occurs at inner aluminum instead of the contacting surface of oxides. **f**, fracture surface after surface relaxation. Oxygen can be injected afterwards for the observation of initial oxidation. Scale bars in (a-b), 5 nm. Scale bars in (c-f), 2 nm.

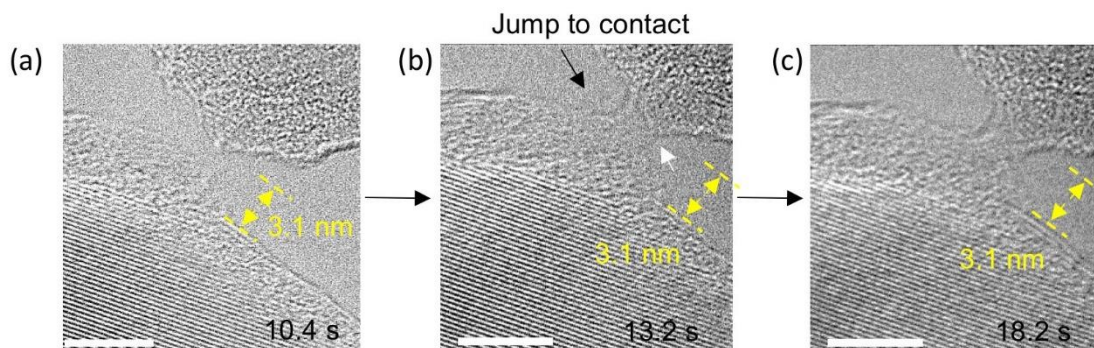


**Figure S3.**

HRTEM images showing aluminum oxide behaves like liquid when the two tips brought to contact. (a) When the two tips are close. (b) Right after oxides jump to contact, necking is formed. The GGI is indicated by the white arrow. (c) Disappearance of GGI. Note that no external forces are applied from (a) to (c). All scale bars, 5 nm. Aluminum atomic planes in HRTEM images are (111).

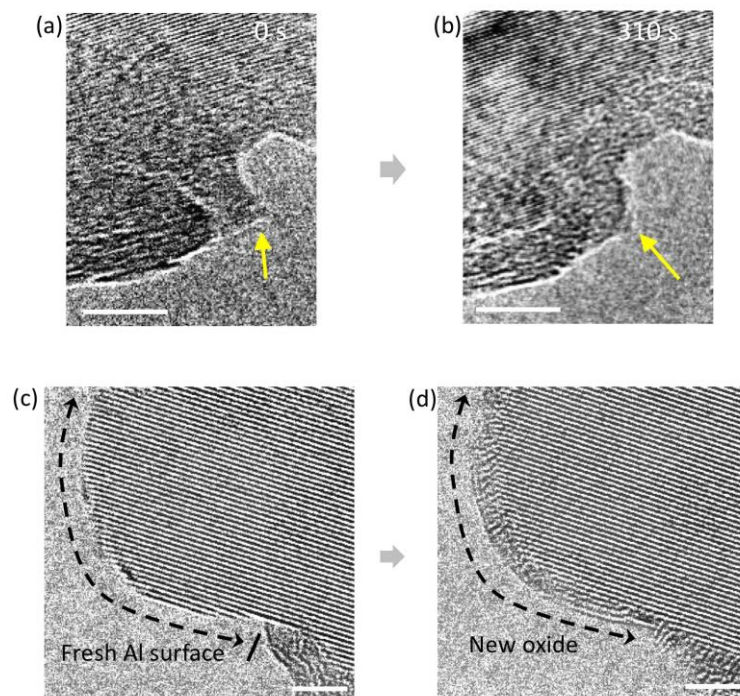


**Figure S4.**

Conformal growth of oxide with smooth M-G interface and G-V interface. **(a-b)**, Sequential HRTEM images showing G-V interface recovers to a smooth shape after deformation. **(c-d)**, Oxide growth on a 90° curved surface of fresh aluminum, rich in various surface inclinations, is still smooth and conformal. All scale bars, 5 nm.

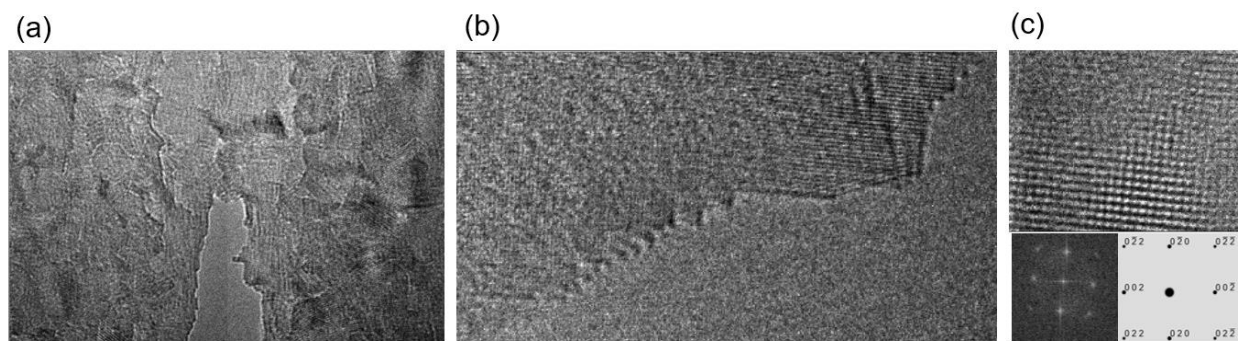


**Figure S5**

HRTEM images of crack tip in a pure (99.99%) magnesium thin film in oxygen environment. (a) The fractures surface is very rough and contains zig-zag facets; oxide grain boundaries are evident. (b) A higher resolution image of the zig-zag surface of MgO. (c) Atomic resolution image showing the lattice of (100) zone axis, with its FFT image showing at the left-bottom corner and diffraction simulation at right-bottom corner.

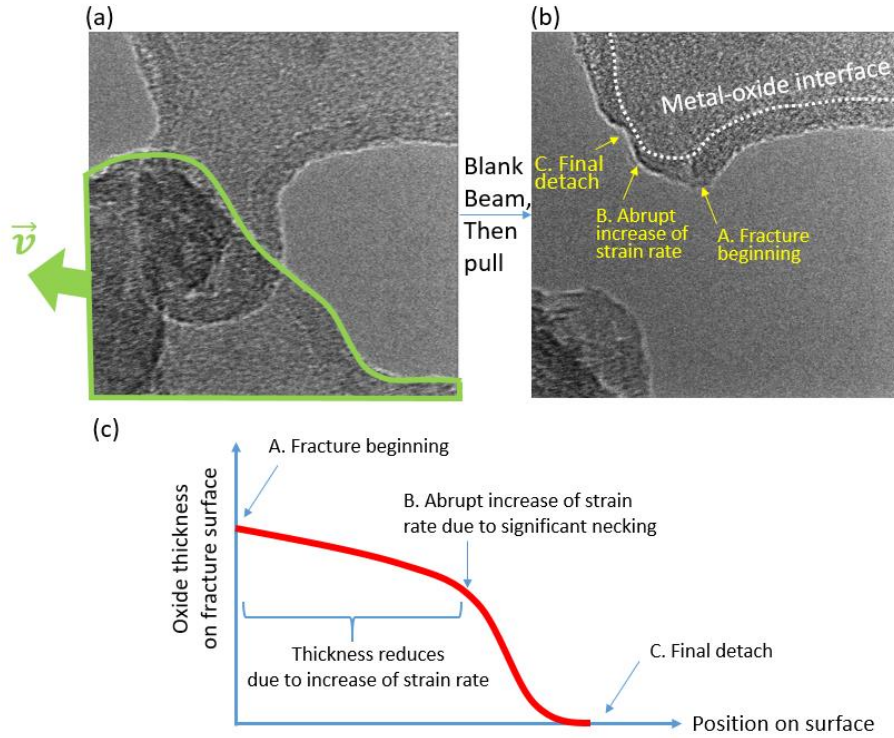


**Figure S6:**

Blanked-beam tearing experiment. (a) Two Al tips are cold-welded. (b) The image taken right after we reopen the beam, showing continuous oxide between point A and point B. (c) Oxide thickness at the fracture surface.

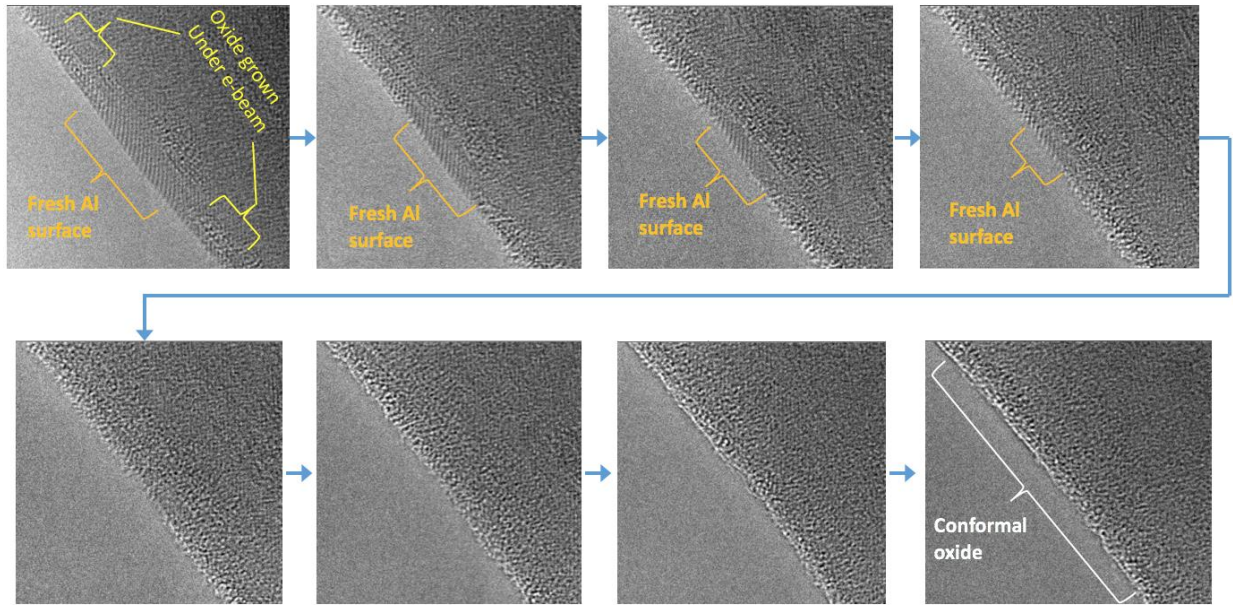


**Figure S7.**

Blanked-beam oxidation experiment: between each frame, the beam is blanked for 30 seconds. The imaging beam flux for each frame is around  $2000 \text{ e}^-/(\text{\AA}^2\cdot\text{s})$ . After taking each snapshot, we blanked the beam immediately.

**Movie S1**

Pulling aluminum oxide in  $2 \times 10^{-6}$  Torr oxygen environment at room temperature.

**Movie S2**

Tearing experiment performed in  $1.5 \times 10^{-1}$  Torr oxygen environment at room temperature.

**Movie S3**

Preparation of clean aluminum surface by pulling the junction at high strain rate.

**Movie S4**

Initial oxidation on aluminum fracture surface under  $3.6 \times 10^{-6}$  Torr oxygen environment.

**Movie S5**

Ultra-low dose-rate experiment for the observation of tearing in an Al nano tip. Oxygen pressure:  $1.5 \times 10^{-1}$  Torr. Dose rate:  $92 \text{ e}^-/(\text{\AA}^2 \cdot \text{s})$ .

## Reference

- (1) Sen, F. G.; Alpas, A. T.; van Duin, A. C. T.; Qi, Y. *Nat. Commun.* **2014**, *5*, 1–9.
- (2) Wünsch, J. R. *Polystyrene: Synthesis, production and applications*; iSmithers Rapra Publishing, 2000; Vol. 112.
- (3) Ellison, C. J.; Torkelson, J. M. *Nat. Mater.* **2003**, *2* (10), 695–700.
- (4) Arhammar, C.; Pietzsch, A.; Bock, N.; Holmstrom, E.; Araujo, C. M.; Grasjo, J.; Zhao, S.; Green, S.; Peery, T.; Hennies, F.; Amerioun, S.; Fohlisch, A.; Schlappa, J.; Schmitt, T.; Strocov, V. N.; Niklasson, G. A.; Wallace, D. C.; Rubensson, J.-E.; Johansson, B.; Ahuja, R. *Proc. Natl. Acad. Sci.* **2011**, *108* (16), 6355–6360.
- (5) Lee, S. K.; Ahn, C. W. *Sci. Rep.* **2014**, *4*.
- (6) Li, J.; Lykotrafitis, G.; Dao, M.; Suresh, S. *Proc. Natl. Acad. Sci. U. S. A.* **2007**, *104* (12), 4937–4942.
- (7) Sun, J.; He, L.; Lo, Y.-C.; Xu, T.; Bi, H.; Sun, L.; Zhang, Z.; Mao, S. X.; Li, J. *Nat. Mater.* **2014**, *13* (11), 1007–1012.
- (8) Krueger, W. H.; Pollack, S. R. *Surf. Sci.* **1972**, *30* (2), 263–279.